Cambridge Books Online

Introduction to Geomagnetically Trapped Radiation

Martin Walt

Chapter

5 - Particle fluxes, distribution functions and radiation belt measure

ments pp. 59-91

5

Particle fluxes, distribution functions and radiation belt measurements

The specification of particle distributions

The preceding chapters have dealt with the motion of an individual particle in magnetic and electric fields. However, the measurement and the description of trapped radiation involves large numbers of particles distributed in space, energy and pitch angle. Hence, the concepts of a distribution function and flux have been introduced to describe the intensity and characteristics of a population of trapped particles.

The particle quantity used to describe trapped radiation intensities, energies and directionality is the particle flux. This quantity is the one most closely related to the output of most space radiation detectors. The differential, directional flux for a given location, direction and energy is the number of particles at energy E within unit dE which cross a unit area perpendicular to the specified direction within a unit solid angle in 1 s. Figure 5.1 illustrates this definition. If dA is the element of area, $d\Omega$ is the element of solid angle in the direction $\hat{\mathbf{e}}_\theta$, and dE is the energy interval at energy E under consideration, the number of particles with energies between E and $E + dE$ passing through dA in the direction $\hat{\mathbf{e}}_\theta$ within $d\Omega$ in 1 s is

$$dN(\mathbf{r}, E, \theta) = j(E, \theta)\, dA\, dE\, d\Omega \qquad (5.1)$$

where $j(E, \theta)$ is the differential, directional flux. (In this definition it is assumed that $d\Omega$ is sufficiently small that all particle velocities are nearly perpendicular to dA.) Note that the plane of area dA through which the particles must pass is perpendicular to $\hat{\mathbf{e}}_\theta$. The customary units of flux are $\mathrm{cm^{-2}\,s^{-1}\,str^{-1}\,keV^{-1}}$, although the energy may be in MeV, keV or eV, depending on the energy range of the particles being described.

In the magnetosphere the most convenient reference direction is the geomagnetic field vector. Hence, the flux direction is usually given by the
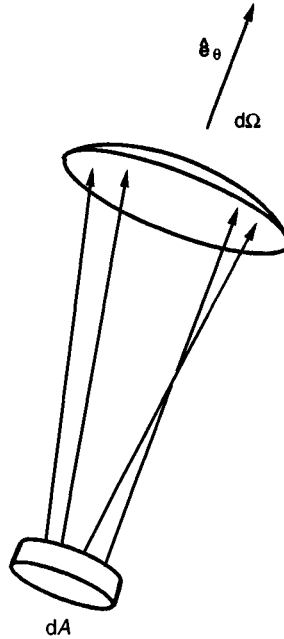
59

Figure 5.1. Illustration of the definition of particle flux in the $\hat{\mathbf{e}}_\theta$ direction.

particle pitch angle. When trapped particle fluxes are symmetrical about the magnetic field line, it is not necessary to indicate the azimuthal dependence of the flux; only the pitch angle (α) dependence is needed. (At locations where the flux has large gradients, such as near the atmosphere or the magnetopause, fluxes will not have this symmetry and the azimuthal variation is needed for a full description.) The pitch-angle distribution of trapped radiation provides clues as to the origin of the particles and their loss mechanisms, as will be described in more detail in Chapter 7. A typical pitch-angle distribution of protons in the stable part of the belt is shown in Figure 5.2. The directional flux is usually a maximum at 90° and falls to nearly zero at the loss cone angle. The flux within the loss cone is very small because these particles will strike the atmosphere before the next reflection and will be removed. The trapped flux is symmetric about 90° since particles at pitch angles of α and 180° $-$ α represent the same population, before and after magnetic mirroring. On a given field line the distribution will vary with latitude since the loss cone angle increases as the observer moves from the equator towards the atmosphere. In Figure 5.2 the upper curve represents the distribution of the integral, directional flux which might be observed in the equatorial plane. The other curves represent flux distributions as seen by a detector
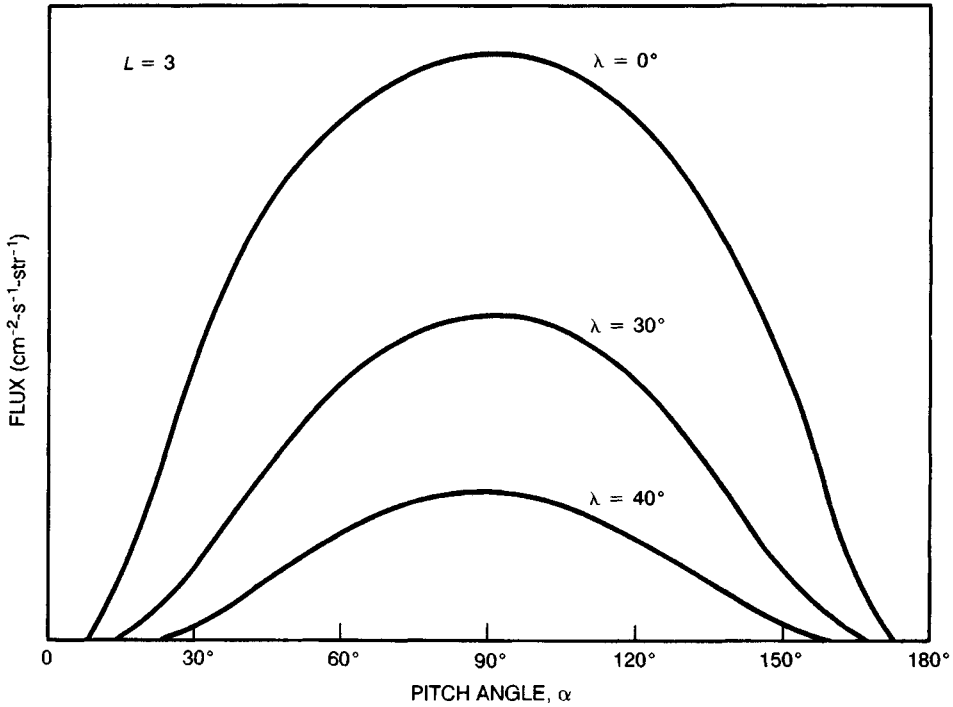
Figure 5.2. Typical pitch-angle distributions at three latitudes on the $L = 3$ field line. As latitude increases, the loss cone angle increases and the flux at 90° pitch angle decreases.

on the same $L = 3$ field line at latitudes of 30° and 40°. The fluxes at each pitch angle are reduced as λ increases, and the loss cone becomes larger with increasing latitude. Later in this chapter it will be shown how the trapped flux in the equatorial plane can be transformed to give flux values at arbitrary positions on the field line.

In this book the differential, directional flux will be designated by $j(\alpha, E)$. Other related flux definitions are

$$\text{Omnidirectional flux} = j(E) = \int_{\Omega} j(E, \alpha)\,d\Omega = \int_{0}^{\pi} j(E, \alpha)2\pi \sin \alpha\,d\alpha$$

(5.2)

$$\text{Integral flux} = j(\alpha, E > E_0) = \int_{E_0}^{\infty} j(\alpha, E)\,dE \qquad (5.3)$$

Although flux is usually plotted as a function of angle, the definition is in terms of solid angle. Hence, all angular integrals of fluxes are taken over solid angle as in the definition for omnidirectional flux in equation (5.2).

The integral flux is the flux above a given energy threshold. Similarly, an integral, omnidirectional flux can be defined by integrating over energy and solid angle to give

$$\text{Integral, omnidirectional flux} = j(E > E_0) = \int_{E_0}^{\infty} dE \int_{0}^{\pi} j(E, \alpha) 2\pi \sin \alpha \, d\alpha$$
(5.4)

Omnidirectional fluxes were often measured in the first years of radiation belt research since the early detectors did not distinguish the direction of arrival of the particles. Today, omnidirectional fluxes are a convenient unit with which to tabulate radiation levels in space since satellite engineers are primarily interested in the overall radiation level which will be encountered.

The integral flux, which is the flux above an energy threshold, is the quantity measured by detectors which respond to particles above a selected energy, determined either by the thickness of shielding material surrounding the sensor of by an electronic bias in the sensor electronics. Again, this flux definition was more appropriate for detectors used in the 1960s and for tabulating flux intensities for engineering purposes. The integral flux may be either directional or omnidirectional.

Note that the definition of differential, directional flux states that the 1 cm^2 area through which particles must pass is perpendicular to the particle velocity. This restriction is important in calculating such quantities as the flux of particles passing through a plane. For example, consider the flux entering the atmosphere in an auroral event in which the downward directed electron flux is isotropic, having filled the loss cone (see Figure 5.3). The downward moving integral flux is independent of α and is equal to j_0 cm^{-2} s^{-1} str^{-1}. We wish to calculate the number of electrons passing through an area of 1 cm^2 perpendicular to the magnetic field.

The number of particles at pitch angle α within a unit solid angle which pass through the unit area perpendicular to **B** is $j_0 \cos \alpha$. Thus the total number of downward moving particles passing through the unit area is

$$N = \int_{0}^{2\pi} d\phi \int_{0}^{\pi/2} j_0 \cos \alpha \sin \alpha \, d\alpha$$
(5.5)

where ϕ is the azimuthal angle. Since j_0 is independent of ϕ and α, the number of particles crossing the unit area perpendicular to **B** is

$$N = j_0 \pi$$
(5.6)

This value is half the value that one would obtain by the incorrect procedure of multiplying the directional flux j_0 by the downward directed solid angle 2π. The factor $\frac{1}{2}$ comes from the definition of flux, namely the
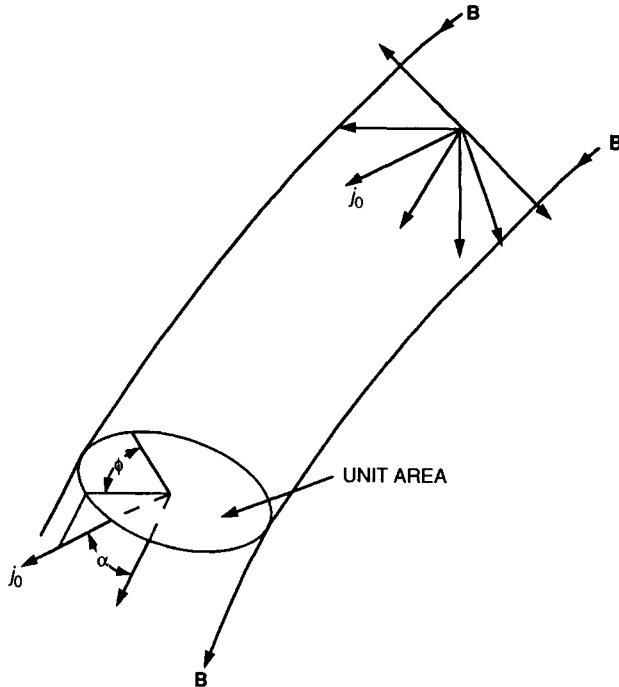
Figure 5.3. Calculation of the particle current across an area perpendicular to **B** in terms of the particle flux, j_o.

number of particles crossing a unit area *perpendicular* to the particle velocity. Since the unit area perpendicular to **B** in Figure 5.3 is not in general perpendicular to the particle direction, the $\cos \alpha$ factor is needed in equation (5.5), resulting in the factor $\frac{1}{2}$.

Another common method of describing particle distributions is in terms of phase space density, a representation which has considerable theoretical importance. The phase space density is the number of particles per unit volume of six-dimensional space composed of the three orthogonal spatial dimensions and the three conjugate momenta. The importance of this coordinate system stems from the central role that phase space density plays in classical and statistical mechanics. For example, Hamilton's equations describe individual particle motion in phase space coordinates, and important theorems exist for these distributions. One of the most useful from the standpoint of space radiation is Liouville's theorem discussed in the next section.

If the particles are non-relativistic, the distribution is sometimes given in terms of velocity rather than energy or momentum. Much of the theory

developed in plasma physics is in terms of a distribution function equal to the number of particles in a unit spatial volume whose velocities lie in a unit volume of velocity space. For non-relativistic particles, velocity space and momentum space differ only by a constant factor. Unfortunately, authors are not always explicit in regard to which distribution function they are using, and the reader must be careful to ascertain the variables involved. In this book distribution functions in phase space variables or adiabatic invariant variables will be denoted by F. All other distribution functions will be designated by f and where confusion is possible the variables will be stated explicitly. For example $f(E, J, L)$ would represent the number of particles per unit dE, dJ and dL at E, J, L.

Liouville's theorem and phase space densities

The adiabatic invariance relationships in Chapter 4 allow one to predict the guiding center trajectories of individual trapped particles. However, the values of fluxes at various positions along the trajectory are also of direct interest. Because of the variation in particle pitch angle during the bounce motion, the convergence of field lines at mirrors, and the irregularities in magnetic shells which are traversed during longitudinal drift, it might be expected that no simple relationship exists between the fluxes at different positions along the path of a particle.

Fortunately, a powerful theorem derived by Liouville can be applied to this question. This theorem will be proved for the case of one spatial dimension and then generalized for three spatial dimensions. Its use for trapped particle geometries will then be illustrated.

Liouville's theorem describes the density of particles in phase space, a space in which the coordinates are the usual spatial coordinates and the conjugate momenta. In the one-dimensional case illustrated here, let the spatial coordinate be q and the conjugate momentum be p (see Figure 5.4). The phase space density of particles is represented by $F(p, q, t)$, which is the number of particles which are at p, q per unit Δp and per unit Δq at time t. The number of particles in the interval q_1 to q_2 and p_1 to p_1 is given by

$$N(t) = \int_{p_1}^{p_2}\!\!\int_{q_1}^{q_2} F(p, q, t)\, dp\, dq \tag{5.7}$$

In Figure 5.4 the number of particles entering the element $\Delta p \Delta q$ in unit time across the left side of the box is $F(p, q)\Delta p \dot{q}(q)$, evaluated at p, q, while the number of particles leaving the element on the right is
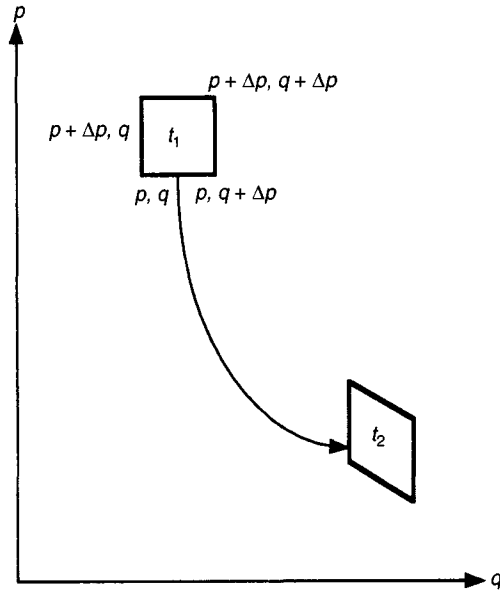
Figure 5.4. Path of a group of particles in one-dimensional phase space. The perimeter enclosing the particle group is distorted but maintains the same area.

$F(p, q + \Delta q)\Delta p\dot{q}(q + \Delta q)$. The difference in these two quantities is the rate at which particles accumulate in the phase space element due to currents across the vertical walls:

$$\frac{\partial F}{\partial t}\bigg|_q \cdot \Delta p \cdot \Delta q = F(p, q)\Delta p\dot{q}|_q - F(p, q)\Delta p\dot{q}|_{q+\Delta q}$$

$$\frac{\partial F}{\partial t}\bigg|_q = \frac{1}{\Delta q}\{F\dot{q}|_q - F\dot{q}|_{q+\Delta q}\}$$

$$= -\frac{\partial}{\partial q}(F\dot{q}) \quad \text{as } \Delta q \to 0 \tag{5.8}$$

Similar considerations apply for the top and bottom walls of the element $\Delta p\Delta q$:

$$\frac{\partial F}{\partial t}\bigg|_p = -\frac{\partial}{\partial p}(F\dot{p}) \tag{5.9}$$

The total rate of increase in the density of particles in the element is the sum of these two terms:

$$\frac{\partial F}{\partial t} = -\frac{\partial}{\partial q}(F\dot{q}) - \frac{\partial}{\partial p}(F\dot{p}) \tag{5.10}$$

Expanding the right-hand side and using Hamilton's equations:

$$\dot{q} = \frac{\partial H}{\partial p}, \; \dot{p} = -\frac{\partial H}{\partial q} \tag{5.11}$$

gives

$$\frac{\partial F}{\partial t} = -\dot{q}\frac{\partial F}{\partial q} - F\frac{\partial \dot{q}}{\partial q} - \dot{p}\frac{\partial F}{\partial p} - F\frac{\partial \dot{p}}{\partial p}$$

$$= -\dot{q}\frac{\partial F}{\partial q} - F\frac{\partial^2 H}{\partial p \partial q} - \dot{p}\frac{\partial F}{\partial p} + F\frac{\partial^2 H}{\partial p \partial q}$$

or

$$\frac{\partial F}{\partial t} + \dot{q}\frac{\partial F}{\partial q} + \dot{p}\frac{\partial F}{\partial p} = 0 = \frac{dF}{dt} \tag{5.12}$$

The total derivative with respect to time is the change in the phase space density of particles as the position in phase space moves with the particles. Equation (5.12) shows that if the individual particle motions can be described by a Hamiltonian, then the phase space density along a dynamical path will remain constant. This extremely useful theorem applies even if the particles change momentum as well as position as a result of the forces.

In Figure 5.4 the particles which are in the phase space volume element t_1 at time t_1 will move to the box labeled t_2 at time t_2. Equation (5.12) indicates that the phase space density of the particles is unchanged. If the forces do not create or destroy particles, then the number of particles in the box at t_2 is equal to the number at t_1. This fact and the equality of particle densities requires that the volume of an element in phase space containing a group of particles is preserved as the particle distribution evolves with time. Therefore, the area of the box at t_2 equals that of the box at t_1, even though the shape at t_2 may be quite distorted.

Equation (5.10) can be generalized to three dimension, the result being

$$\frac{dF(q_1, q_2, q_3 : p_1, p_2, p_3; t)}{dt} = \frac{dF(\mathbf{q}, \mathbf{p}, t)}{dt}$$

$$= \frac{\partial F}{\partial t} + \sum_{i=1}^{3}\frac{\partial F}{\partial q_i}\dot{q}_i + \sum_{i=1}^{3}\frac{\partial F}{\partial p_i}\dot{p}_i = 0 \tag{5.13}$$

In trapped radiation research the particle populations are usually described in terms of fluxes rather than phase space densities. Hence, to apply Liouville's theorem it is necessary to relate flux to phase space density. This relationship will be derived by describing the number of particles crossing an area per unit time in terms of flux and in terms of phase space density. Equating these two quantities will then give the desired relationship.

Consider an area dA whose plane is perpendicular to $\mathbf{v}$ and calculate the number of particles passing through dA s^{-1} in the direction of $\mathbf{v}$ within $d\Omega$ (see Figure 5.5).

In terms of flux $j(\theta, E)$ the number is

$$dN = dA \cdot j \cdot d\Omega \, dE$$

$$= dx \, dy \cdot j \, d\Omega \cdot \frac{p}{m} \, dp \tag{5.14}$$

In terms of phase space density, $F(\mathbf{p}, \mathbf{q})$, the number of particles crossing dA in one second is

$$dN = F \cdot dx \, dy \, dz \cdot dp_x \, dp_y \, dp_z$$

$$= F \cdot dx \, dy v \cdot p^2 \, d\Omega \, dp \tag{5.15}$$

where $dz = v$ ($\Delta t = 1$ s) is the length of the configuration space volume passing through dA in 1 s. The momentum space volume is the shell of thickness dp depicted in Figure 5.5.

Equating (5.14) and (5.15) gives

$$F(\mathbf{q}, \mathbf{p}) = j(\theta, E)/p^2 \tag{5.16}$$

Although the derivation given here is non-relativistic, the result is relativistically correct. The significance of this result combined with Liouville's theorem is readily apparent. Where p^2 is constant, the flux does not vary along a dynamical path. Therefore, in the steady state the observed differential, directional flux at any position along the dynamical path of a
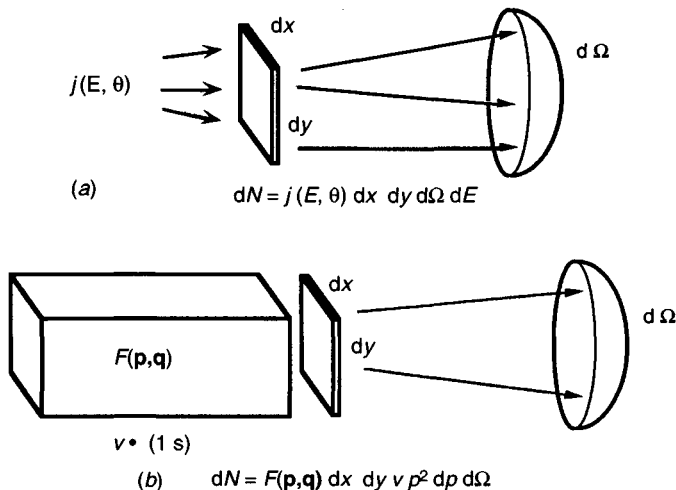

Figure 5.5. Description of a particle distribution in terms of flux (a) and phase space density (b).

bounce trajectory or a drift trajectory will be numerically equal. Thus, in the absence of time variations flux measurements at the same B, I values in the magnetosphere will give identical results. Even at different B and I values the directional fluxes will be identical if the two points are on a particle trajectory.

As an illustration of this flux equality, consider the pitch-angle distributions in Figure 5.2. These distributions are on the same field line but are at different latitudes and hence have different values of the magnetic field. At any latitude λ the directional flux at pitch angle $\alpha(\lambda)$ is equal to the equatorial flux at pitch angle α_{eq} where

$$\alpha_{eq} = \sin^{-1}(\sqrt{[B_{eq}/B(\lambda)]}\sin\alpha(\lambda)) \tag{5.17}$$

Thus, in Figure 5.2 the flux at $\alpha = 90°$, $\lambda = 40°$ is equal to the flux at $\alpha = 40.6°$, $\lambda = 30°$ and is equal to the flux at $\alpha = 21.6°$, $\lambda = 0°$. By applying Liouville's theorem and the conservation of the magnetic moment, the pitch-angle distribution at any point on the field line can be mapped from the distribution at the equatorial plane. However, the procedure cannot be reversed to derive a complete equatorial distribution from measurements made at higher latitudes since the high-latitude data do not include information on particles mirroring between the equator and the measurement point.

The explanation for the equality of flux at various positions on a field line is quite simple. As one moves from the equator into higher B, the solid angle containing a group of particles expands, diluting the flux. This effect is exactly compensated by the converging magnetic field which brings more particles into a unit area perpendicular to the field line.

Trapped radiation measurement techniques

In general a charged particle detector consists of a sensor, which records the impact of a particle, and a collimator, which shields the detector from particles whose velocities are not within the desired solid angle (Figure 5.6). The sensor may measure the energy of particles striking it and thereby allow the energy spectrum to be measured. The sensor may consist of many active elements to increase the information obtained from a detection event. The collimator or entrance aperture may contain electric or magnetic analysis elements which will only allow the passage of particles of a given type or energy. If the sensor has area A cm^2 and the collimator has an acceptance solid angle of Ω steradians pointing in the direction α with respect to **B**, the counting rate of particles with energies
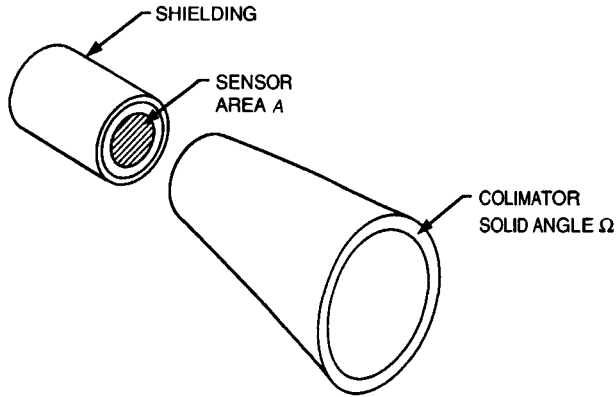
Figure 5.6. Generic charged particle detector consisting of a shielded sensor and an entrance collimator.

between E and $E + dE$ will be

$$\text{Counting rate} = j(\alpha, E)A\Omega\,dE \tag{5.18}$$

In equation (5.18) it is assumed that Ω is sufficiently small that all particles striking the sensor are moving perpendicular to A and that the variation of j over Ω is negligible. The more general case will be treated below. The combination $A\Omega = G$ is called the geometric factor of the detector. The geometric factor, whose units are expressed in cm^2 steradians, is a measure of the sensitivity of the detector. The larger the geometric factor the higher the counting rate in a given flux. The geometric factor should include a factor for the counting efficiency of the sensor. Here it will be assumed that all particles striking the sensor will initiate counts so that the efficiency is unity.

In designing experiments the geometric factor is selected to achieve a sufficiently large counting rate that statistical errors are small. If n is the number of counts recorded in an accumulation cycle and $n \gg 1$, the statistical error or standard deviation in the count value is $n^{\frac{1}{2}}$. The fractional error is therefore $n^{\frac{1}{2}}/n$, which becomes smaller as n increases. However, increasing n by enlarging either component of the geometric factor entails costs. If Ω is large, the angular resolution of the measurement suffers. A larger sensor area A increases the overall size and weight of the detector and collimator and increases the shielding weight required. Thus, the various parameters for the detector must be adjusted to optimize the experiment. Since fluxes vary greatly with position, angle and energy, it is not usually possible to design a detector that has good response under all the conditions that it will encounter in space.

Detectors using electrostatic or magnetic analysis have geometric factors which vary with energy. If $G(E)$ is the geometric factor at energy E, the counting rate is given by

$$\text{Counting rate} = \int_0^\infty j(E, \alpha) G(E) \, dE \qquad (5.19)$$

The counting rate will therefore depend on the value of the flux in the acceptance energy window of the detector. For the geometric factor shown in Figure 5.7, the counting rate will describe the flux in the interval between E_1 and E_2. Altering the energy of the window by adjusting the electrostatic or electromagnetic analysis sections of the detector will shift the window and allow the energy spectrum to be explored.

The energy spectrum can also be obtained directly using sensors whose output pulse amplitudes are related to the energy deposited in the sensor by the particle. The output pulses are fed to a pulse height analyzer which evaluates the energy of each particle, thus constructing an energy spectrum.

If the acceptance angle Ω is so large that the flux is not uniform over the aperture, integration is necessary to relate the counting rate to the flux. In Figure 5.8 let the vertical axis be in the direction of the magnetic field and the detector axis at angle θ with respect to the magnetic field. The detector of area A has a half-angle of acceptance of β and the acceptance solid angle is represented by a circle of radius β drawn on the unit sphere.
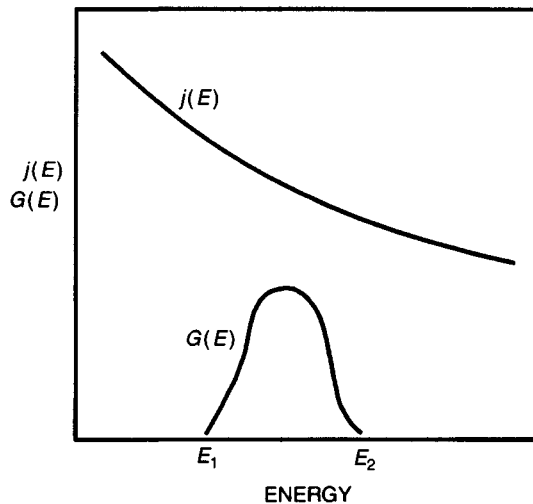

Figure 5.7. With an energy-dependent geomagnetic factor $G(E)$, the detector will sample the particle flux $j(E)$ at energies between E_1 and E_2.
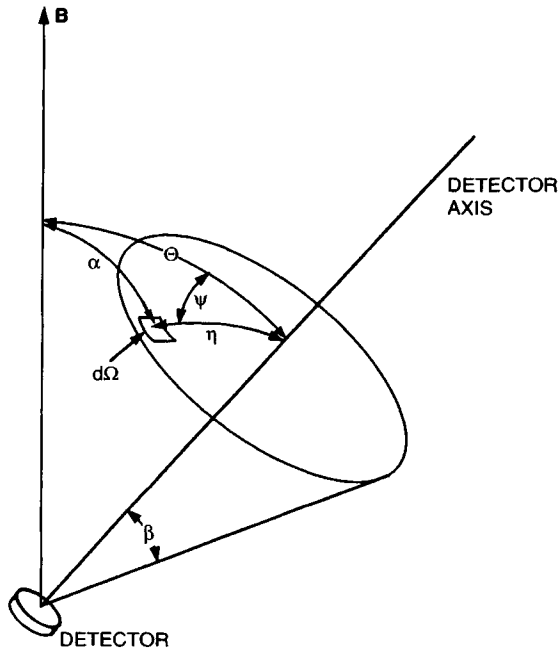
Figure 5.8. Geometry for calculating detector counting rates when the directional flux varies over the acceptance solid angle of the detector.

The flux is a function of pitch angle α, and integration of the flux over Ω is needed to obtain the counting rate. The differential of solid angle is

$$d\Omega = \sin \eta \, d\eta \, d\psi \qquad (5.20)$$

The counting rate for an integral flux of $j(\alpha, E > E_{th})$ is

$$C.R. \, (E > E_{th}) = \int_0^{2\pi}\int_0^{\beta} j(\alpha, E > E_{th}) \cdot A \sin \eta \, d\eta \, d\psi \qquad (5.21)$$

In the integrand α is a function of η, θ and ψ given implicitly by the cosine law for spherical triangles:

$$\cos \alpha = \cos \theta \cos \eta + \sin \theta \sin \eta \cos \psi \qquad (5.22)$$

In the general case this integral must be evaluated numerically. In practice, one often expresses $j(\alpha, E)$ as a function of several parameters and adjusts the parameters to fit experimental counting rates.

Particle detectors

After the discovery of the radiation belts the techniques for measuring particle fluxes evolved rapidly, more or less in step with satellite technology and solid state electronics. The first measurements were taken

using Geiger–Müller counters, which consist of gas-filled cylinders with center wires maintained at a large positive voltage with respect to the cylinder walls. A charged particle traversing the gas volume produces free electrons which are accelerated towards the center wire where the large electric field creates an avalanche of ions and electrons. The movement of these ions and electrons in the electric field of the counter reduces the voltage between the center wire and the wall. This voltage pulse indicates the passage of a charged particle through the counter. These devices are inexpensive and reliable but are limited in their dynamic range and give no information on the energy or type of particle or photon producing the initial ionization. In cases where the fluxes are known to be mostly electrons or protons, some energy information can be obtained if several identical counters, each surrounded by a different thickness of shielding material, are used. The range–energy relationship of electrons or protons in the shielding material determines the energy threshold for the detector, and these integral flux measurements at several thresholds give a crude estimate of the energy spectrum of the flux being observed.

In the 1960s Geiger–Müller counters were replaced by scintillation detectors and solid state sensors. In both of these types of particle detector the amplitude of the output signal, the light pulse from the scintillator or the current pulse from the solid state detector, is proportional to the energy deposited in the sensor material. For sensors large enough to stop the incoming particle, the pulse amplitude distribution of output pulses gives a direct measurement of the energy spectrum of the incident particles. Both scintillation counters and solid state sensors can sustain higher counting rates than can Geiger–Müller counters and therefore have greater dynamic ranges.

More elaborate detector systems having multiple sensors and discrimination elements are now common. A popular configuration is a two-element telescope consisting of a thin dE/dx sensor followed by a larger total energy detector. The thin element gives the energy loss per unit distance traversed in the material and the final detector measures the total energy deposited by the particle. These two quantities suffice to determine energy and particle identity, since dE/dx for a singly charged particle depends primarily on the particle's velocity. Knowing the velocity and energy leads to determination of the mass. Such telescopes easily distinguish electrons from ions, and in some versions can separate protons from helium or heavier ions. Added elements can be used to improve particle identification and discriminate against background. For example, a shield of active material, either a scintillator or solid state detector surrounding

the counting system except for the entrance aperture, can be operated in anti-coincidence with the central detector and will reject signals from particles which do not enter through the aperture. Figure 5.9 illustrates an example of this type of particle spectrometer. The total energy sensor consists of a stack of silicon solid state detectors whose output signals are added to give a total energy pulse.

To detect low-energy particles which cannot penetrate the covers, light shields or dead layers of scintillators or solid state detectors, channel multiplier sensors are appropriate. The sensing element consists of a hollow tube whose interior is lined with a material having a low work function. A voltage of approximately 1 kV is applied between the ends of the tubes. An electron or ion entering the open end (negative potential) will strike the walls and initiate a cascade of electrons towards the positive end of the tube. At the positive end this electron cloud is collected, the charge is fed to an amplifier and the pulse is passed on to the detection logic. Since any charged particle or a photon can initiate a cascade the channel multiplier cannot discriminate between particle type or energy, and any particle analysis must be done prior to detection. Thus, ahead of the sensor are magnetic or electrostatic spectrometers or both. Combined magnetic and electrostatic analysis is a powerful technique since the former element separates particles by momentum and the latter by energy, thus leading to unambiguous determination of particle mass if the charge is known. In practice, these detectors vary the applied electric or magnetic fields in order to scan the energy and mass of the incoming particle flux.
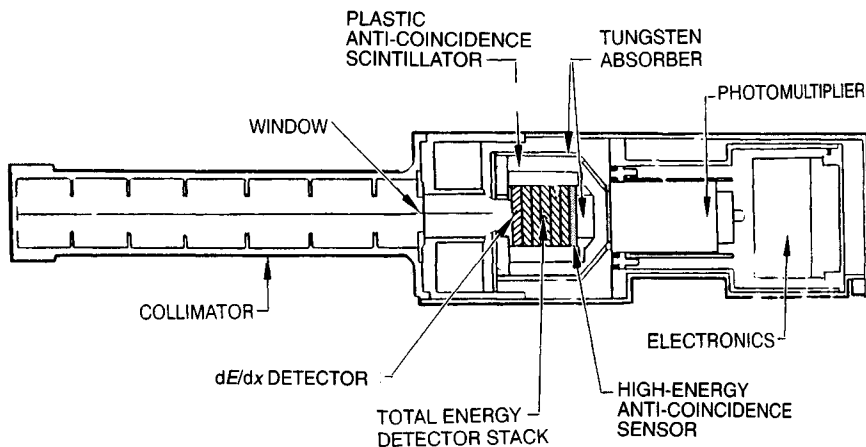

Figure 5.9. Highly directional particle spectrometer which will identify the particle species and measure the particle energy.

Arrays of channel multipliers, called channel plates, offer the possibility of recording an image of the incoming particle flux. Depending on the analysis elements which proceed the detector, the position of a particle when it strikes the channel plate can represent two characteristics, such as energy and angle of arrival or mass and energy. A relatively simple use of the channel plate is to place it behind a small aperture, with or without magnetic or electrostatic focusing, so that the position of detection on the plate records the direction of arrival of the particle. Such a detector gives high angular resolution for studying flux distributions with large angular gradients.

Solid state detectors are also used in arrays for detector focal planes. In addition to particle trajectory information which is given by the detector location, the energy of the particle is obtained if the detector is thick, and dE/dx is recorded if the detector is thin. Again, a combination of dE/dx, total energy and anti-coincidence shielding elements can be combined to yield information on the flux, particle type, energy spectra and angular distribution.

Trapped particle populations

Introduction

The purpose of this section is to outline the general characteristics of the Earth's radiation belts by describing the species, energy spectra, and spatial distributions of the trapped particles. It is important to have a general understanding of the types and distributions of radiation belt particles in order to appreciate their scope and the physical processes which take place. More complete models of the belts are available in publications by NASA, from which the information presented here was derived. The NASA models give parametric representations of the fluxes, and the values of the parameters are tabulated. These data and the computer programs available from NASA allow rapid computation of the fluxes of electrons and protons at any position within the radiation belts. If one knows the ephemeris of a satellite, one can then calculate the radiation it would encounter at all points in its orbit, and by integrating over time one can find the accumulated dose received during its life in space.

Over the years since 1958, trapped radiation measurements have been made by many satellites using a variety of detectors. In spite of this wealth of data, our knowledge of radiation belt characteristics is still incomplete.

Before 1975 many of the measurements were made with detectors with poor energy sensitivity and which were unable to discriminate between protons and electrons. Also, the geometric factors of some detectors were often uncertain, making it difficult to derive accurate flux values from the counting rates. Finally, the time variations of flux values in the belts are large, and the intensity and energy spectra vary with time of day, magnetic activity and solar cycle phase. Under these conditions it is difficult to evaluate average values for flux levels.

The particle populations described below have been derived by NASA from careful examination of data taken from a large number of independent experiments. Where necessary, interpolations and extrapolations were made to fill data gaps. While it is difficult to estimate errors, it is likely that errors of a factor of 3 are common, and errors of an order of magnitude may occur where large flux gradients exist. Also, because of the large time variations, the actual flux measured at any particular time may differ by an order of magnitude from the average values provided by these models.

In recognition of the need for better radiation belt models, the CRRES (Combined Release and Radiation Effects Satellite) was launched in 1990. This mission was equipped with modern particle detectors and obtained data for nine months as it traversed the belts in an eccentric, equatorial orbit. These data are now being incorporated into improved radiation belt models and should be available in a few years.

It is customary to describe the radiation belts as consisting of two zones, an inner zone for the region inside $L \approx 2.5$ and an outer zone for $L \gtrsim 2.5$. This terminology was adopted when the early detectors experienced counting rate maxima at about $L = 1.5$ and $L = 3.5$ with a minimum or 'slot' in between. This topology results from an intense flux of high-energy protons at $L = 1.5$ and a broad maxima of energetic electrons near $L = 3.5$. The region of the minima, $L = 2.0$–2.5, is termed the slot region, to designate the relative absence of energetic particles.

Radiation belt protons

Energetic protons are found throughout the region of the magnetosphere where the geomagnetic field will sustain trapping. Contours of the omnidirectional, integral flux of protons above 100 keV are shown in Figure 5.10, where the intensity contours are plotted in the r–λ coordinate system. The maximum flux occurs on the equatorial plane at about $L = 3.1$. On this plot, which depicts averages, the maximum flux along
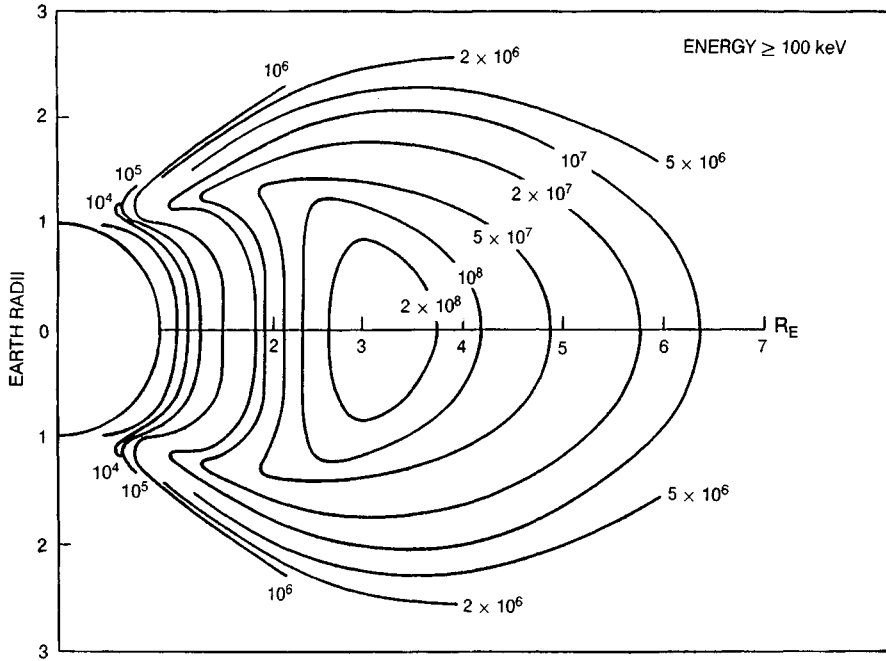
Figure 5.10. Omnidirectional, integral proton flux with energy greater than 100 keV. Based on data supplied by the National Space Science Data Center.

any L value will be found at the equator. The intensity contours become more closely spaced below $L = 1.5$, where the Earth's atmosphere becomes dense enough to remove the energetic protons.

Distributions are shown in Figure 5.11 for protons above 10 MeV and in Figure 5.12 for energies above 50 MeV. As the energy threshold increases, the flux maximum moves closer to the Earth. The increase in the average energy of trapped particles with decreasing L is a general characteristic of the radiation belts and will be discussed in Chapters 8 and 9. In these data, which are based on many experiments, the proton distribution displays a single maximum. Some experiments have reported transient secondary maxima, indicating that at times the proton distribution exhibits more structure than is shown here.

Proton energies extend up to several hundred MeV, making the proton fluxes the most penetrating of all trapped particles. Figure 5.13 illustrates the differential energy spectrum above 17 MeV. The extremely large energies, much larger than any electrical potentials occurring within the magnetosphere, suggest the existence of an energy source other than the electric and magnetic fields associated with the Earth.
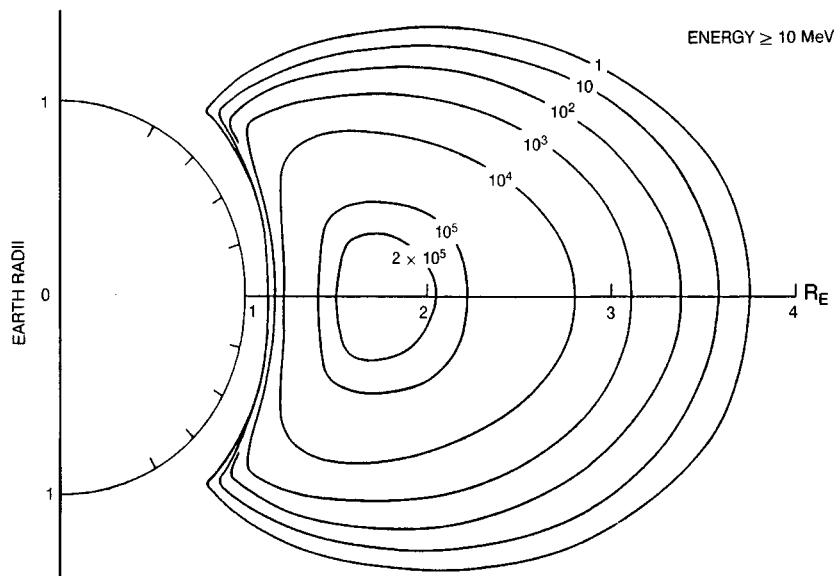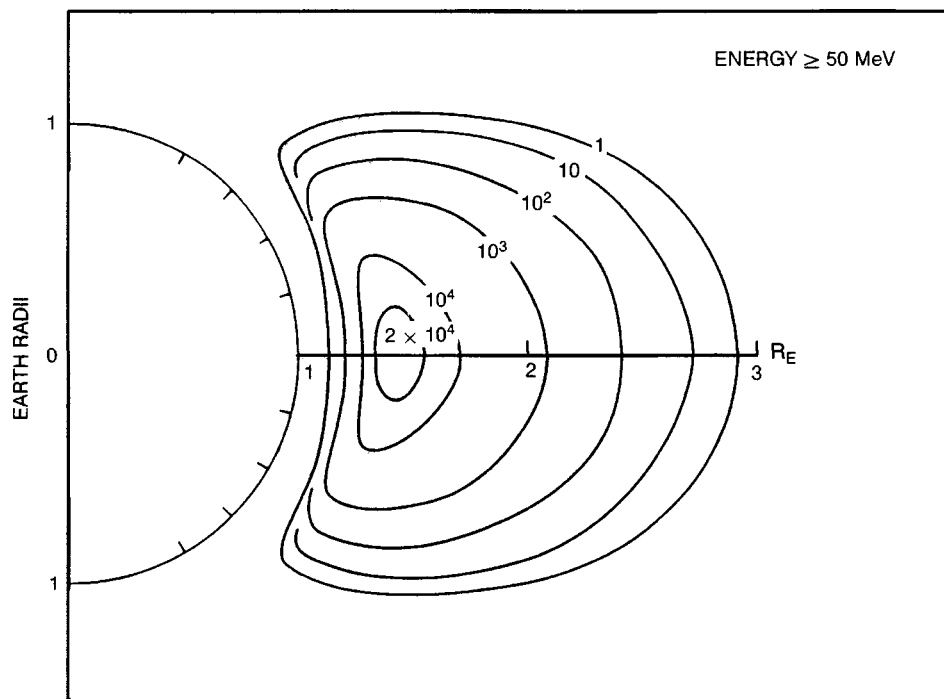
Figure 5.11. Omnidirectional, integral proton flux with energy greater than 10 MeV. Based on data supplied by the National Space Science Data Center.

Figure 5.12. Omnidirectional, integral proton flux with energy greater than 50 MeV. Based on data supplied by the National Space Science Data Center.
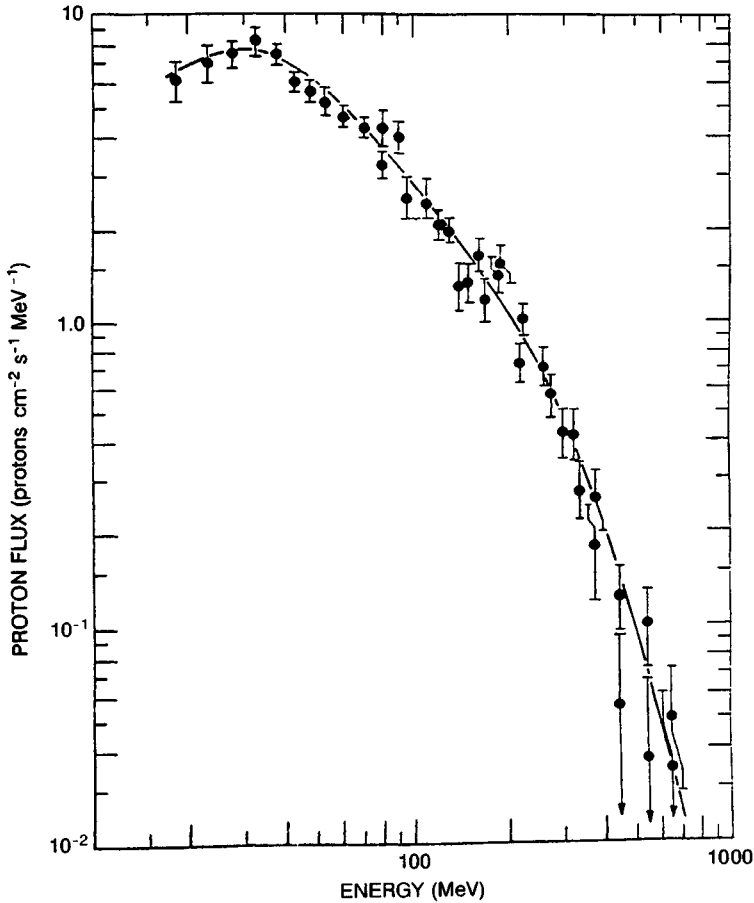
Figure 5.13. Differential energy spectrum of protons in the inner radiation zone.

The concentration of very high-energy protons near the Earth makes these particles the primary radiation hazard for satellites in low Earth orbit. At low altitudes, asymmetries in the geomagnetic field distort the contours of radiation intensity. As the particles drift around the Earth, their mirroring points follow lines of constant B and L. The altitude of these lines varies with longitude and differs in the northern and southern hemispheres because of the distortion of the magnetic field. In particular, the region in the southern hemisphere between South America and Africa is notable for the weak value of the surface magnetic field. In order to mirror at a constant B value, particles must descend to lower altitudes while drifting over this region. Thus, for a given altitude, the radiation intensity is much higher over the South Atlantic anomaly section than
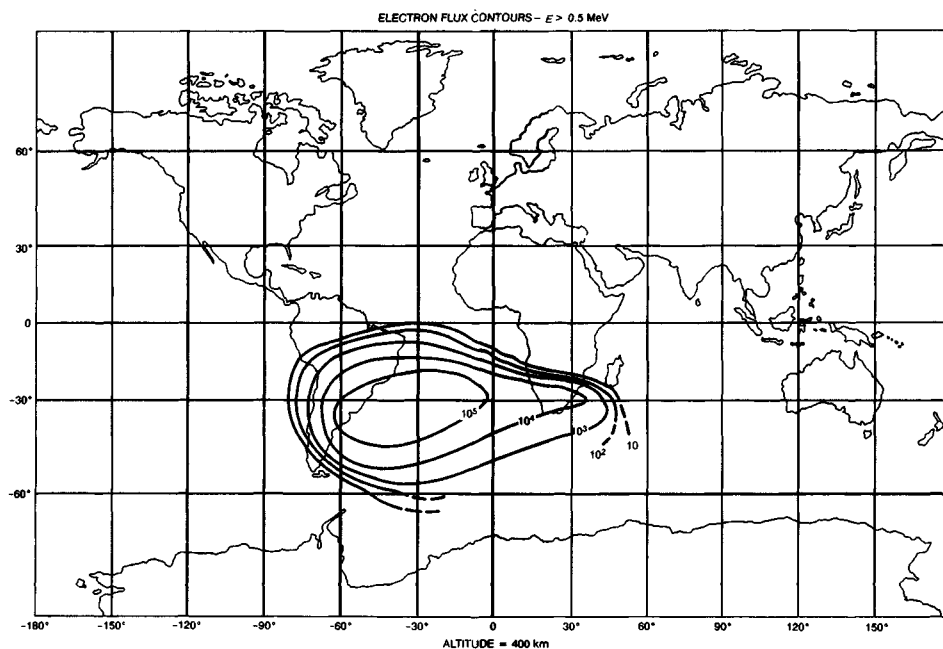
Figure 5.14. Radiation concentration at the South Atlantic anomaly. Isointensity contours of electrons above 0.5 MeV at an altitude of 400 km.

elsewhere. This effect is illustrated in Figure 5.14, which shows the radiation intensity of electrons with energies above 0.5 MeV at an altitude of 400 km. Contours of isointensity lines show the concentration of flux near the magnetic anomaly and indicate the importance of that region for satellite damage considerations.

Electrons

Energetic electrons occur throughout the Earth's trapping region and have energies extending up to several MeV. The fluxes exhibit time variations related to geomagnetic activity, and the average fluxes change during the solar cycle. As a result of this latter effect, different models are used for periods of solar maximum and solar minimum to bracket the expected average flux values. Because of the warping of the geomagnetic field by the solar wind, fluxes above $L = 5$ exhibit a local time variation that is incorporated in the models.

Figure 5.15 gives the equatorial values of integral, omnidirectional electron fluxes for a number of energy thresholds. The important features
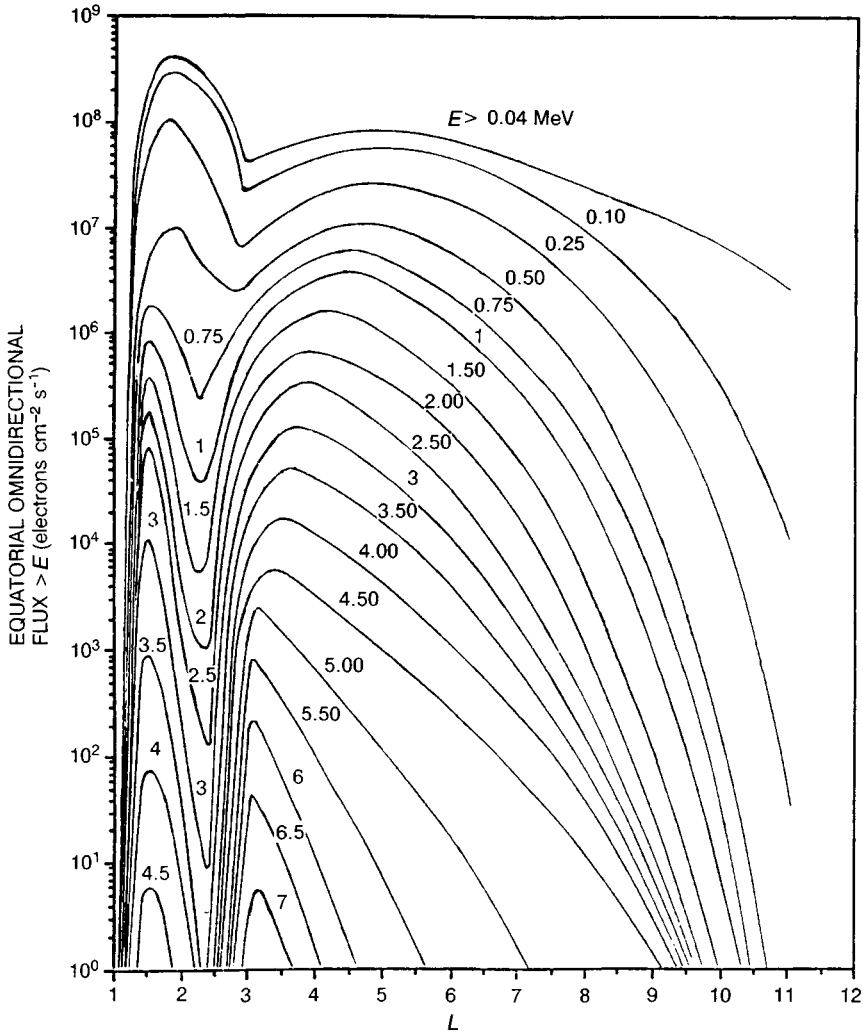
Figure 5.15. Equatorial values of the integral, omnidirectional electron flux above various energy thresholds. Based on data supplied by the National Space Science Data Center.

to note are the rapid decrease in flux with increasing energy, the concentration of high-energy electrons at the lower L values, and the slot region at $L \approx 2.5$. The slot, which is more pronounced for the higher-energy electrons, is believed to result from enhanced electron loss rates in this region.

Contour plots in $r-\lambda$ coordinates are given in Figures 5.16–5.18 for integral omnidirectional fluxes above 40 keV, 1 MeV and 5 MeV. In the
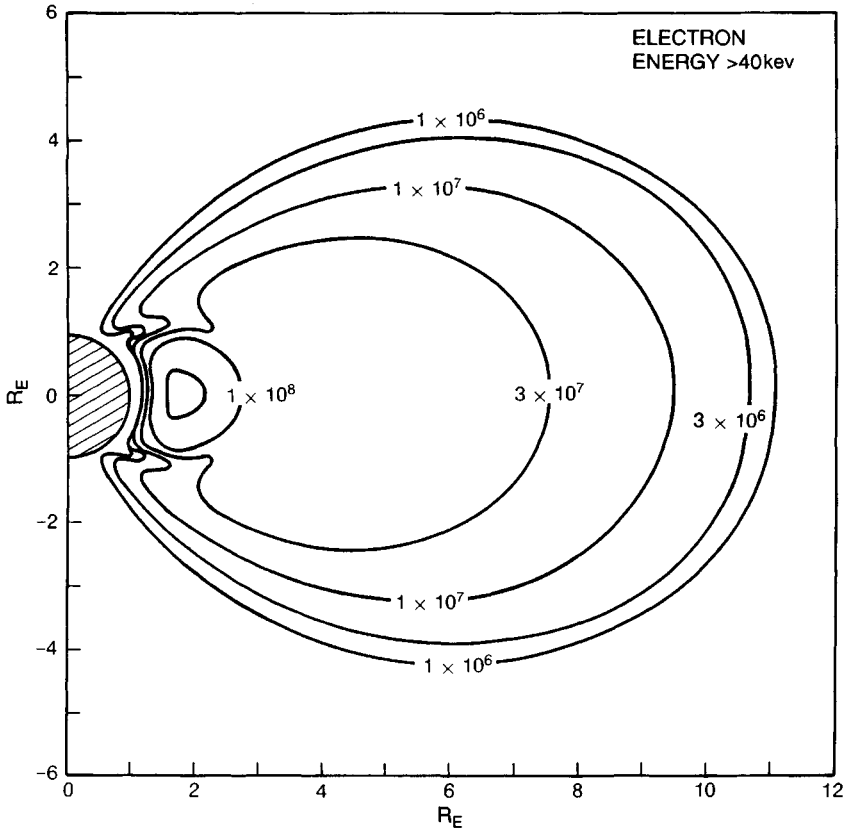
Figure 5.16. Integral, omnidirectional electron flux greater than 40 kev. Based on data supplied by the National Space Science Data Center.

first two diagrams the slot region is quite apparent. At L values of 3–5 the high-energy electrons are the most penetrating, and therefore the most damaging, component of the radiation belts.

Ions other than protons

In addition to electrons and protons the radiation belts contain significant components of heavier ions. The most abundant of these are helium and oxygen, although fluxes of carbon and nitrogen have also been identified. The most energetic of these heavy ions, with energies of a few MeV, have maxima in their radial distributions near $L = 3$ and have equatorial pitch-angle distributions which are sharply peaked near 90°. Therefore, the particles remain near the equatorial plane. At lower energies,
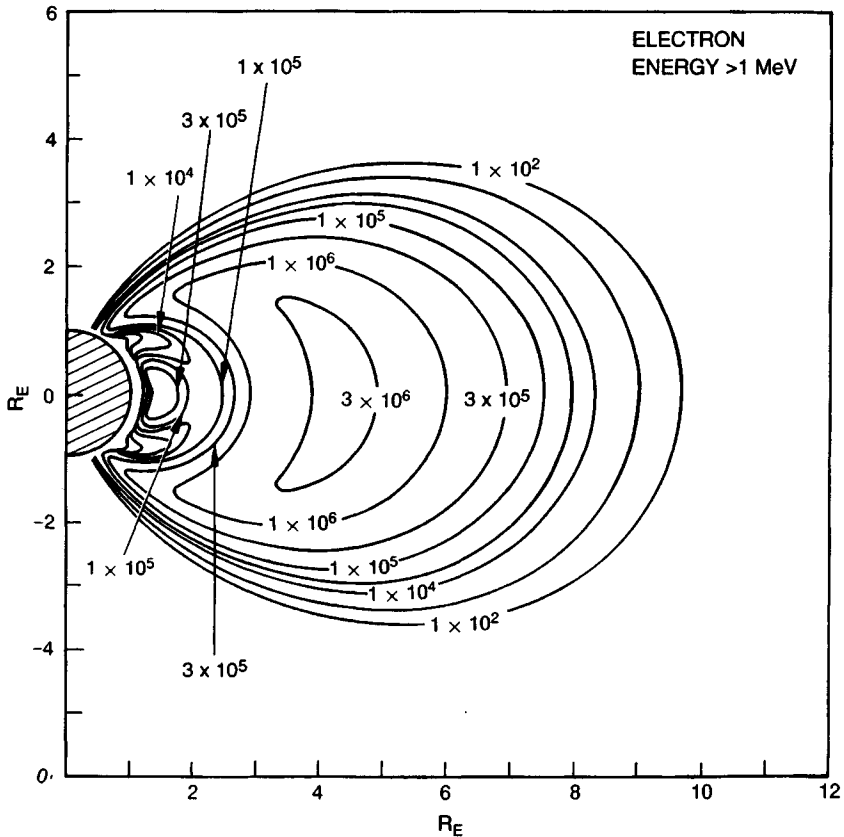
Figure 5.17. Integral, omnidirectional electron flux greater than 1 MeV. Based on data supplied by the National Space Science Data Center.

1–50 keV, oxygen and helium ions are quite abundant, particularly during magnetically active periods. There is strong evidence that these ions are drawn out of the atmosphere at high latitudes, and during substorms are accelerated and moved inward to $L = 3$ to 4. Occasionally, oxygen ions are the principal component of the ring current.

The presence of helium and oxygen ions trapped in the magnetosphere has led to important insights as to the origins of trapped particles and the physical processes responsible for the acceleration and trapping of ions. The singly charged oxygen ions must come from the Earth's ionosphere. Hence theories on the formation of the radiation belts must contain elements which permit the acceleration and trapping of the cold iono-spheric plasma.
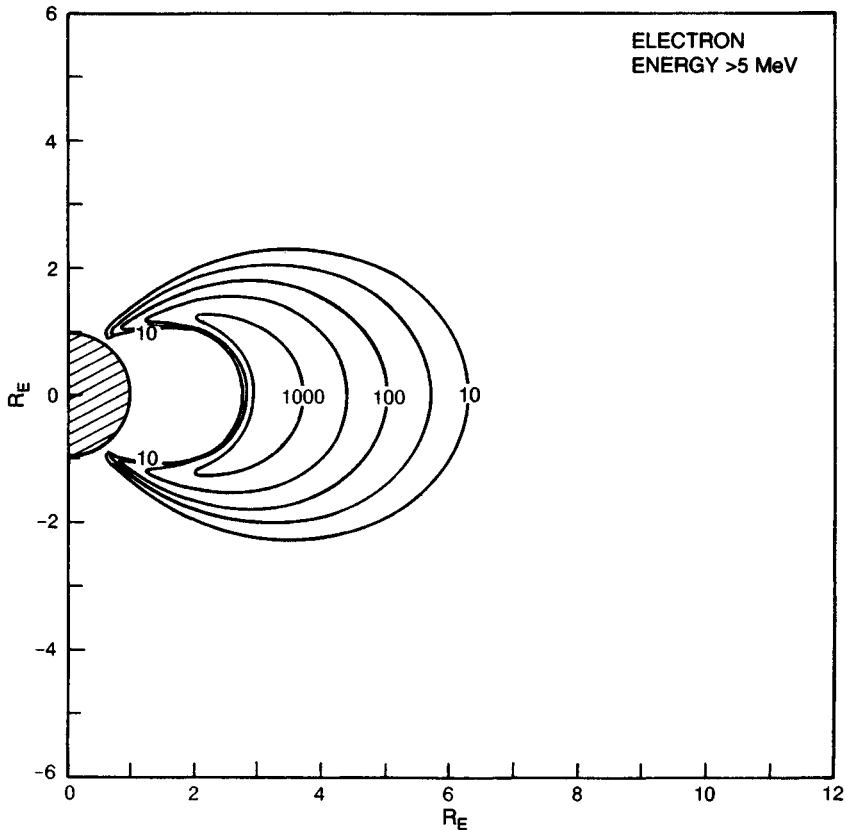
Figure 5.18. Integral, omnidirectional electron flux greater than 5 MeV. Based on data supplied by the National Space Science Data Center.

Time variations

All components of the radiation belts, both ions and electrons, exhibit time variations in flux intensity, energy spectra and spatial distributions. These variations are a major reason for the difficulty of mapping average values for satellite design purposes. Time variations are dominated by magnetic activity. Major magnetic storms produce changes throughout the trapping region, although the changes are largest in the outer zone. Magnetic substorms are more frequent but less severe disturbances in the geomagnetic field. During a substorm the configuration of the geomagnetic tail becomes less distorted and the induction electric fields modify the trapped particle distributions. Some of these changes are reversible. For example, symmetric compression of the geomagnetic field

followed by a relaxation to the initial configuration causes only a temporary change in trapped particle distributions. However, asymmetric compressions lead to the movement of particles across L shells and a concomitant acceleration.

The mechanisms by which magnetic storms and substorms affect the radiation belts are not fully understood. Some of the processes will be described in more detail in Chapters 8 and 9. Here, examples of observations will be presented to indicate the magnitude and characteristics of the observed variations.

High-energy protons are those components of the radiation belts that are least affected by geomagnetic activity, largely because they reside in the inner radiation belt where fractional changes in B are smallest. Also, protons with energies approaching 100 MeV are less sensitive to induction electric fields whose integrals along the proton drift path are usually much less than 1 MeV. An illuminating example of the impact of a magnetic storm on the integral omnidirectional flux of protons above 34 MeV is shown in Figure 5.19. The data depict the fluxes at various L values above $L = 1.9$ before and after a magnetic storm which took place on 23 September, 1963. While the flux at $L = 1.9$ is unaffected, the change becomes progressively larger with increasing L. Although such large
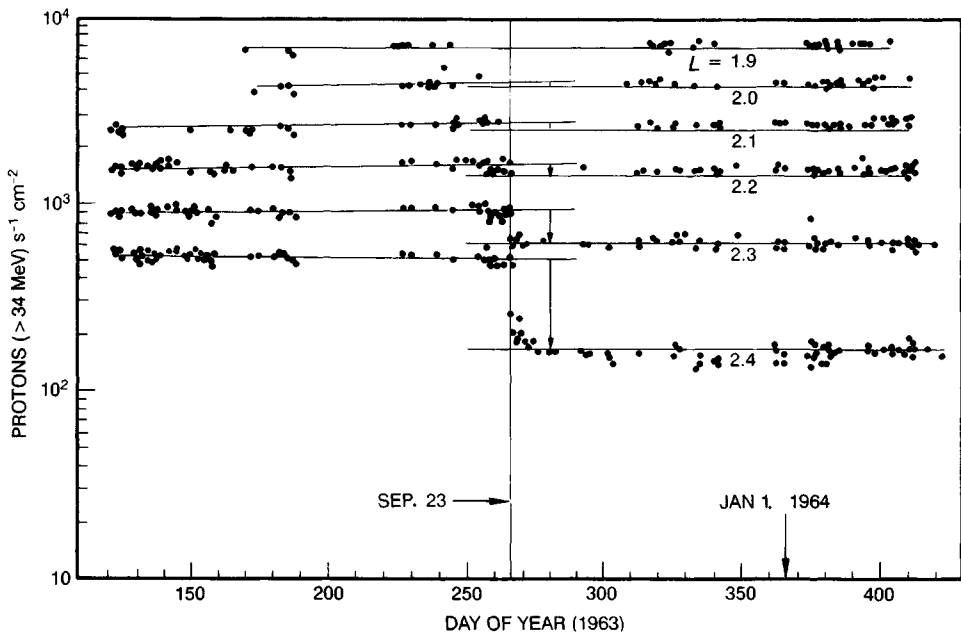

Figure 5.19. Sudden changes in high-energy proton fluxes caused by a major magnetic storm.

storms are rare, the long lifetimes of high-energy protons imply that they will experience a number of these storms.

At lower energies and higher L values the changes are more severe and complex. Figure 5.20 illustrates proton fluxes above several energy thresholds at $L = 4$. The storm which occurred on day 109 increased the flux at 2 MeV by an order of magnitude. In subsequent weeks following the storm, redistribution of the protons continued.

Electron fluxes are also susceptible to time variations, particularly in the outer radiation zone. The time behavior of 1 MeV electrons at L values between 3 and 5.5 is shown in Figure 5.21. The lowest panel of the diagram is a plot of the magnetic index, D_{st}, which indicates magnetic storms, and K_p, which is a measure of auroral activity at high latitudes. A decrease in D_{st} occurs during the main phase of a magnetic storm. Note
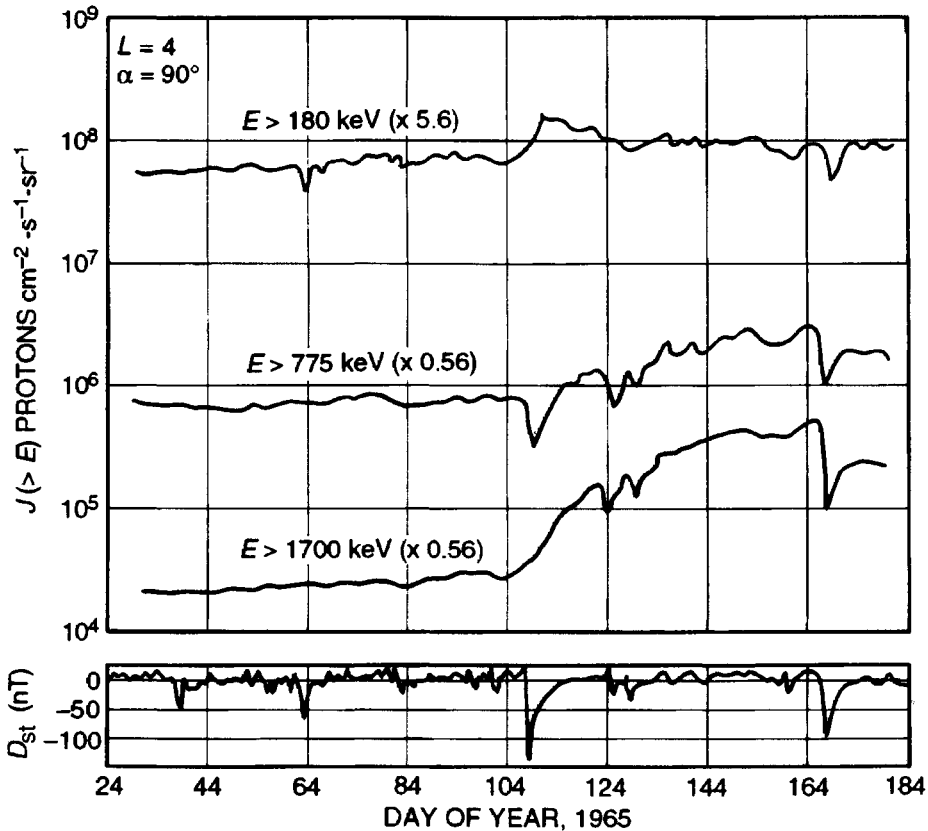

Figure 5.20. Variations in the integral, directional proton flux above three energy thresholds at $L = 4$. The lower panel gives the magnetic D_{st} index: a low value of D_{st} indicates a geomagnetic storm.
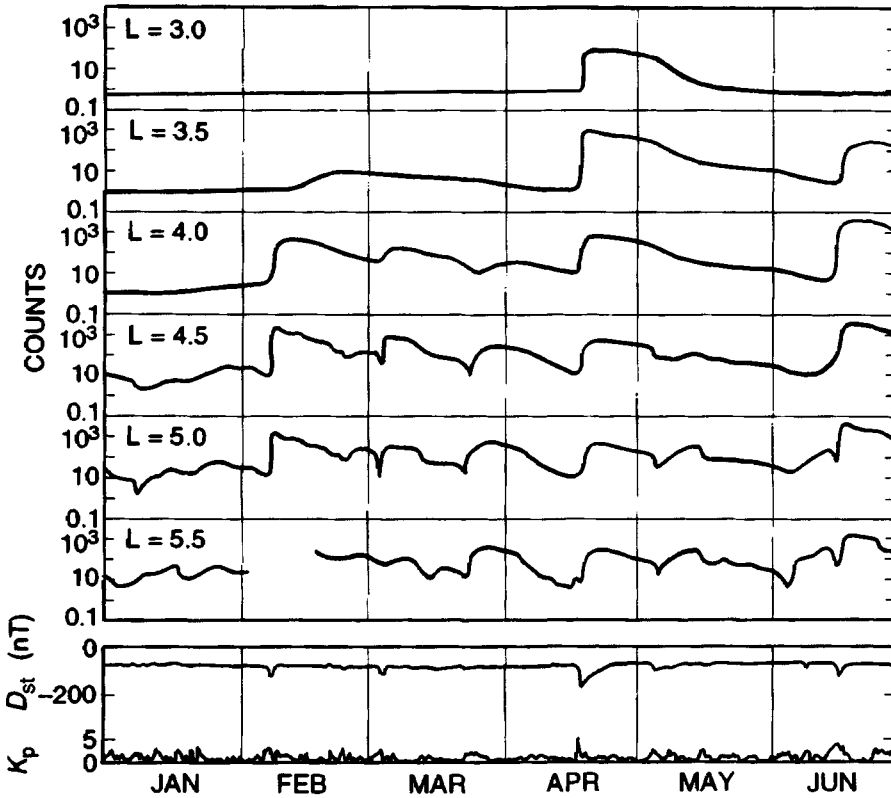
Figure 5.21. Effect of magnetic activity on electrons with energies above about 1 MeV. Lower panels give the magnetic storm index D_{st} and the planetary magnetic activity index K_p. Note the correlation of D_{st} depressions with increases in trapped electron flux.

that each magnetic storm results in a substantial increase in the trapped flux. During the weeks following the storm, the flux decays approximately exponentially with time. Strong auroral activity, on the other hand, is often associated with a reduction in trapped electron flux.

The morphology of the time variations in radiation belt distributions is one of the most puzzling features of the trapping phenomena. Ultimately, the dynamic behavior of the particle fluxes will be understood in terms of the electric and magnetic field variations which are imposed by magnetospheric conditions or are generated by the particles themselves.

Problems

1. An auroral scientist observes the intensity of the 391.4 nm line in a stable aurora and determines that 1 erg cm^{-2} s^{-1} of energy is being deposited in the

atmosphere. From the altitude of the luminosity he also estimates that the energy of the electrons entering the atmosphere is 5 keV. If he assumes that the flux entering the atmosphere is isotropic, find the integral, directional electron flux which would be measured in the loss cone by a satellite at the equator (1 eV $= 1.6 \times 10^{-12}$ erg).

2. A directional proton spectrometer measures the proton flux at a point in space and obtains

$$j(\alpha) = 4 \times 10^2 \exp\left(-E/E_0\right)\sin^3\alpha \quad (\text{cm}^{-2}\,\text{s}^{-1}\,\text{str}^{-1}\,\text{MeV}^{-1})$$

where α is the pitch angle and $E_0 = 10$ MeV:

(a) What is the omnidirectional flux above $E = 0$?
(b) What is the omnidirectional flux above 30 MeV?

3. A satellite designer finds that a CMOS integrated circuit installed in a satellite ready for launch will be damaged by energetic protons during the expected lifetime of the satellite. Because of weight restrictions she can only shield the circuit over 2π steradians. However, since the satellite is stabilized in attitude, she can place the 2π steradians of shielding in the most effective geometry. If the integral proton flux has an angular distribution of

$$j(\alpha) = C\sin^4\alpha \quad (\text{cm}^{-2}\,\text{s}^{-1}\,\text{str}^{-1})$$

what is the fraction of the original flux that can be excluded? The satellite is to be in a circular orbit at the equator.

4. An engineer is designing a proton detector to measure protons of energy greater than 10 MeV using a scintillation counter with a pulse height threshold of 10 MeV. He wishes to have an angular resolution of ± 5 degrees and designs the collimator to this value. If the expected flux is 2×10^5 protons cm^{-2} s^{-1} str^{-1} for $E > 10$ MeV and his count accumulation time is 200 ms, what is the area of the detector surface needed to achieve 1% statistical accuracy (standard deviation) in one accumulation interval?

5. Following a magnetic storm the integral electron flux above 100 keV measured on the equator over the Pacific at $L = 2$ is isotropic above a drift loss cone angle of 30°, the cut-off resulting from the low field values at the South Atlantic magnetic anomaly.

   Find, for $L = 2$ at the longitude of the measurement given in the diagram below:

(a) The omnidirectional flux on the equator.
(b) The omnidirectional flux at a magnetic latitude of 30° (assume dipole field).
(c) When the distribution drifts to the Atlantic side of the Earth, will the equatorial omnidirectional flux be smaller, larger, or the same (assume no L-shell splitting)?
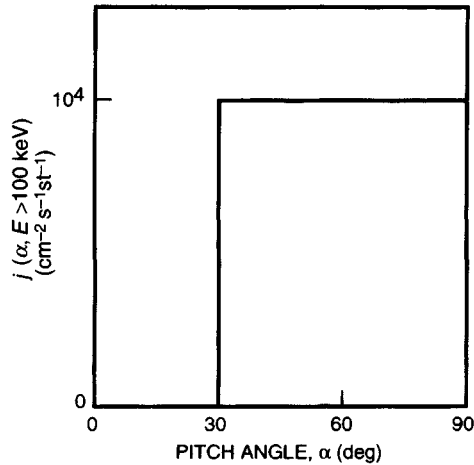
6. A magnetic mirror machine used for controlled fusion experiments has the configuration shown below. The field is symmetric about the z axis and is expressed in cylindrical coordinates. The z component is $B_z = B_0 e^{\alpha z^2}$. Charged particles with a radius of gyration much less than the dimensions of the machine will oscillate between mirroring points and slowly drift about the central axis:
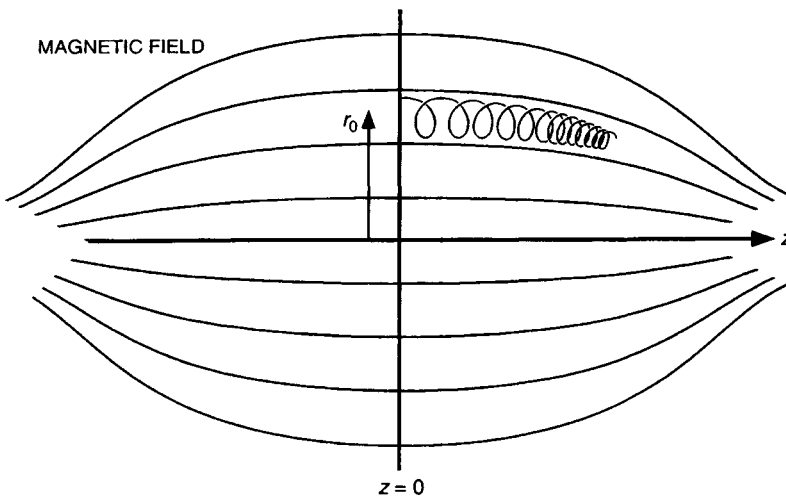

(a) Find the radial component of the field.
(b) A particle trapped between the magnetic mirrors at the ends of the configuration has its guiding center at a distance r_0 from the axis when passing $z = 0$. What is the third adiabatic invariant of the particle?

7. On the left-hand side of the diagram given below a differential, directional flux of protons

$$j(E, \alpha) = CE^{-2} \quad (\text{cm}^{-2}\,\text{s}^{-1}\,\text{str}^{-1}\,\text{keV}^{-1})$$

is uniform over pitch angles from 0 to 90°. The protons are accelerated by a potential difference V_0 and continue towards the right. Derive an expression for the flux on the right at pitch angle $\alpha = 0$ and energy E_0. Express the answer in terms of E_0, C, V_0 and q (charge on the proton).
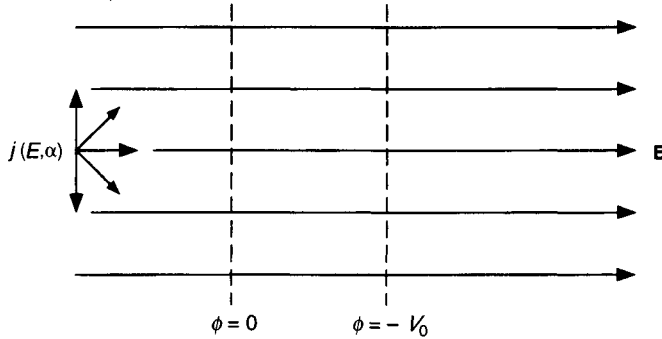
8. In the magnetic field configuration shown below a particle detector in B_1 measures the flux moving towards the right above some threshold energy and finds an angular distribution which is constant over the angular interval 0–90°. No measurements are made beyond 90°. Sketch the angular distribution of the flux from 0 to 180° at B_1, B_2 and B_3. Assume that all fluxes are time independent:
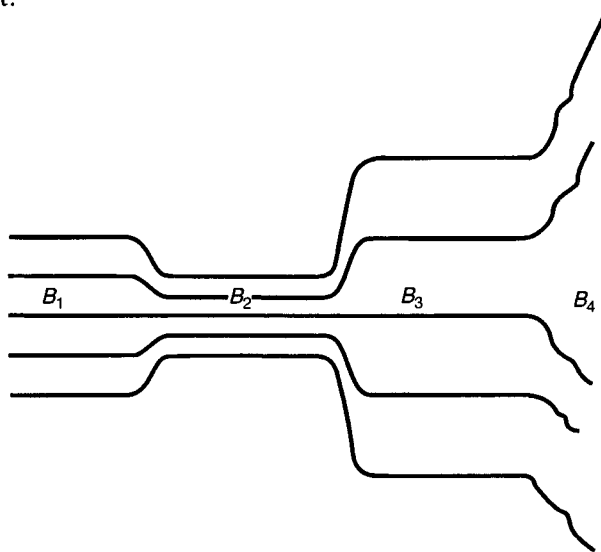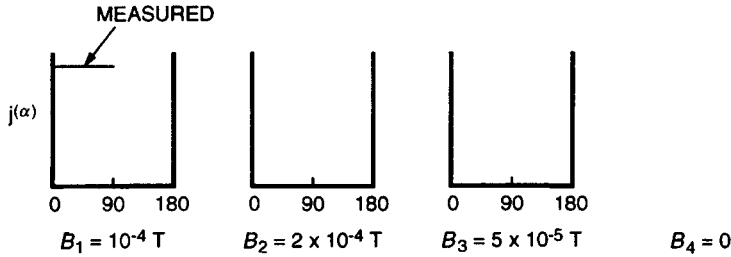

$$B_1 = 10^{-4} \text{ tesla}$$
$$B_2 = 2 \times 10^{-4} \text{ tesla}$$
$$B_3 = 5 \times 10^{-5} \text{ tesla}$$
$$B_4 = 0$$

MEASURED

$j(\alpha)$

| 0   90   180 | 0   90   180 | 0   90   180 | |
| $B_1 = 10^{-4}$ T | $B_2 = 2 \times 10^{-4}$ T | $B_3 = 5 \times 10^{-5}$ T | $B_4 = 0$ |

9. The geometric factor of an electron spectrometer is designed to be 0.05 cm² str in order to attain the necessary counting rate in an expected isotropic flux:

(a) If the collimator has a half-angle of 10°, what is the area of the detector?

(b) A new estimate of the isotropic flux reduces its value by a factor $\frac{1}{2}$. If the instrument builder cannot increase the size of the detector, to what angle must the collimator be changed?

10. A satellite with a unique guidance system is controlled to follow a magnetic field line at $L = 3$ from the equator to 40° in latitude. It carries an omnidirectional proton detector which accumulates counts for 10 s at the equator, at 20° latitude, and at 40° latitude:

(a) Assuming that the loss cone angle is defined by the solid earth, is the detector response consistent with the flux being isotropic outside the loss cone?*

Counts at equator	1010 counts in 10 s
Counts at 20° latitude	972 counts in 10 s
Counts at 40° latitude	895 counts in 10 s

(b) If the detectors were much more sensitive and had the following response, would the results be consistent with isotropy outside the loss cone?

Counts at equator	9.89×10^5 counts in 10 s
Counts at 20° latitude	$9.8 \ \times 10^5$ counts in 10 s
Counts at 40° latitude	$8.8 \ \times 10^5$ counts in 10 s

* If N is the number of counts accumulated in some time interval, the probable error in N due to counting statistics is $\sqrt{N}$ for large N.

11. By 2020 AD NASA has learned to control the magnetic moment of the Earth by energizing subterranean magnets. In an effort to protect communication satellites, NASA decides to remove all trapped radiation below $L = 1.5$. However, there is only enough power to operate the magnets for a few hours so the changes to the Earth's magnetic field will be temporary:

(a) Should NASA increase or decrease the Earth's magnetic moment for a few hours?

(b) By what factor should the Earth's magnetic moment be changed in that period? (Assume the Earth's field is a centered dipole with the field given by

$$\mathbf{B} = \frac{\mu_0}{4\pi} \frac{\mathcal{M}}{r^3}(-2\cos\theta\hat{\mathbf{e}}_r - \sin\theta\hat{\mathbf{e}}_\theta)$$

and neglect the atmosphere.)

12. At the equatorial plane a satellite observes an isotropic flux of electrons for $E > 5$ keV and $j(E < 5 \text{ keV}) = 0$:

$$j(\alpha, E) = 10^5 \, (E_0/E)^3 \text{ electrons } (\text{cm}^2 \text{ s str keV})^{-1}$$

where $E_0 = 1$ keV:

(a) What is the value of the omnidirectional, integral flux above 5 keV?
(b) If the satellite is at $L = 2$, what is the loss cone angle (neglect the atmosphere)?
(c) What is the value of the power going into the atmosphere per cm^2 at the end of the field line?